Detecting mid-infrared light by molecular frequency upconversion with dual-wavelength hybrid nanoantennas

Angelos Xomalis [1], Xuezhi Zheng [1,2], Rohit Chikkaraddy [1], Zsuzsanna Koczor-Benda [3], Ermanno Miele [1,4,5], Edina Rosta [3], Guy A E Vandenbosch [2], Alejandro Martínez [6], Jeremy J Baumberg [1*]

[1] NanoPhotonics Centre, Cavendish Laboratory, Department of Physics, University of Cambridge, Cambridge, United Kingdom.
[2] Department of Electrical Engineering (ESAT-TELEMIC), KU Leuven, Leuven, Belgium
[3] Department of Physics and Astronomy, University College London, London, United Kingdom
[4] Department of Chemistry, University of Cambridge, Cambridge, United Kingdom
[5] The Faraday Institution, Harwell Science and Innovation Campus, Oxford, United Kingdom
[6] Nanophotonics Technology Center, Universitat Politècnica de València, Valencia, Spain

*Corresponding author. email: jjb12@cam.ac.uk

ABSTRACT

Coherent interconversion of signals between optical and mechanical domains is enabled by optomechanical interactions. Extreme light-matter coupling produced by confining light to nanoscale mode volumes can then access single mid-infrared (MIR) photon sensitivity. Here we utilise the infrared absorption and Raman activity of molecular vibrations in plasmonic nanocavities to demonstrate frequency upconversion. We convert $\lambda \sim$10 μm incoming light to visible via surface-enhanced Raman scattering (SERS) in doubly-resonant antennas that enhance upconversion by >10^{10}. We show >200% amplification of the SERS antiStokes emission when a MIR pump is tuned to a molecular vibrational frequency, obtaining lowest detectable powers ∼1 μW/μm^2 at room temperature. These results have potential for low-cost and large-scale infrared detectors and spectroscopic techniques, and bring single-molecule sensing into the infrared.

One-Sentence Summary:

Molecules as Mixers.

Detecting weak mid-infrared light currently requires expensive cooled devices. Xomalis *et al* instead convert the light to visible frequencies where it is efficiently measured, by using vibrating molecules inside a cavity that traps the multiple frequencies of light simultaneously. Using self-assembled devices integrated onto silicon wafers, they exploit the nonlinear interaction of mechanical vibrations and oscillations of light. This yields the first successful devices in the recently emerging field of molecular optomechanics.

Infrared spectroscopy delivers information hard to obtain from other frequency bands, such as atmospheric absorption of molecules (greenhouse gases) or thermally-emitted radiation

from earth (meteorological maps or imaging wildfires) (*1-5*). While development of mid-IR (MIR) sources evolves, a bottleneck continues to be in producing low-noise room-temperature detectors (*6*). One proposed scheme is to directly upconvert MIR photons into high-energy visible photons that are efficiently detected, potentially delivering single-photon semiconductor-based detectors (*7-9*). Analogous wavelength conversion from microwave to optical frequencies has utilised expensive fabrication and cryogenic temperatures (*10, 11*), as well as $LiNbO_3$ resonators (*12, 13*). Critically, in order to access the efficiencies required, strongly-enhanced light-matter interactions are paramount. Thus, plasmonic devices and planar resonant metasurfaces which confine light have been of interest for MIR integrated detection and biosensing (*14-16*).

A promising approach for detecting infrared radiation through frequency upconversion is via molecular optomechanical coupling (*17*). Optomechanical interactions allow coherent conversion of signals between optical and mechanical domains (Fig. 1). Nanocavities containing vibrating molecules act as mechanical oscillators, with MIR-absorbing infrared vibrational modes probed by a visible laser through their Raman scattering (Fig. 1B). The required interactions can be boosted by using the tight light localisation inside plasmonic nanocavities <100nm across which yield detectable signals even from single vibrational bonds (*18*). The interaction of light and matter in these sub-nm mode volumes gives extreme optomechanical coupling with single MIR-photon sensitivity in principle, but so far only studied theoretically (*17*). The noise-equivalent power of hybrid nanocavity-molecular detectors is predicted to be hundred-fold lower than commercial uncooled detectors.

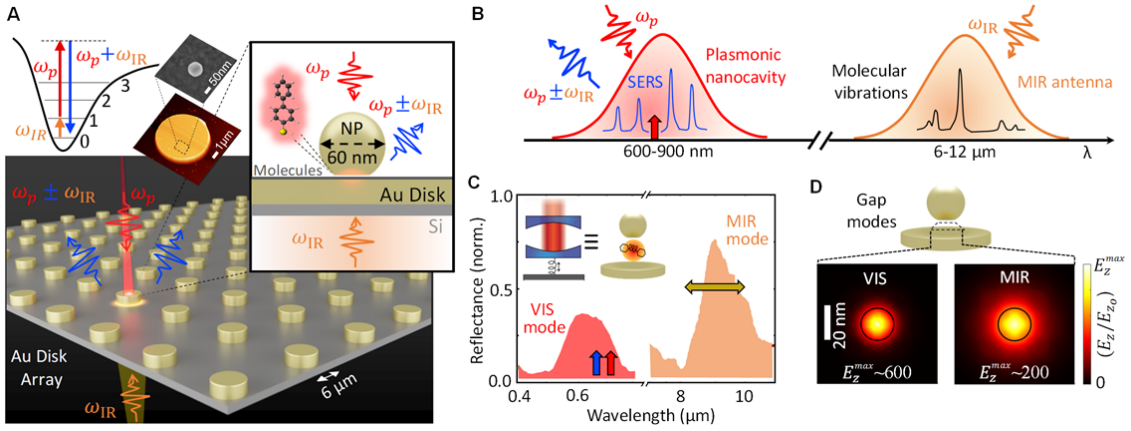

Fig. 1. Dual-wavelength antenna and frequency upconversion. (**A**) Pump (MIR) - probe (visible) detection configuration. Inset shows upconversion process, AFM (disk) and SEM (nanoparticle) images, and self-assembled monolayer of biphenyl-4-thiol which creates 1.3nm cavity between 60nm Au nanoparticle and 6µm disk. (**B**) Scheme of MIR to visible up-conversion via molecular optomechanics. (**C**) Experimental reflectance of NPoR resonances at both visible (red) and MIR (orange) wavelengths. Arrows indicate SERS probe wavelength (785nm, red), inelastic scattered light (blue) and MIR tuning range (8.5-12.6µm, yellow). Inset shows equivalence of optomechanical cavity and NPoR. (**D**) Near-field normalised maps of mid-infrared (MIR) and visible gap modes of NPoR. Black circle shows 20 nm nanoparticle facet.

Of vital importance for upconversion efficiency is the optimal spatial overlap of visible and infrared radiation. Plasmonics allows extreme light confinement at visible frequencies, but at longer wavelengths light localisation drops significantly. Achieving light confinement simultaneously in both visible and MIR spectral regions requires a hybrid dual resonator (*19*). Here, this is fulfilled by creating doubly-resonant antennas which focus long- and short-wavelengths into the same active region allowing good optomechanical coupling (Fig. 1D). Their construction combines bottom-up and top-down methods that allow for ease of fabrication and cost-effective large-scale arrays of devices.

To demonstrate MIR detection, we perform surface-enhanced Raman spectroscopy (SERS) on self-assembled molecular monolayers (SAMs) with discrete vibrational absorption modes in the λ=6-12µm range. Coupling requires matching the optical (infrared absorption) and mechanical (molecular vibration) energies. Biphenyl-4-thiol (BPT) is chosen (inset Fig. 1A) since it provides vibrations that are simultaneously active in both IR absorption and Raman, and binds strongly and consistently to gold. Integrated into a dual-wavelength gold antenna, the nanoparticle-on-resonator (NPoR), this strongly confines visible and MIR within the same active region (*19*), accessing single-molecule optomechanical nonlinearities (*20, 21*). The Au disk resonators (diameter 6µm) have a fundamental resonant mode around λ=10µm and high order modes in the visible (*19*). Onto these is self-assembled a molecular monolayer of BPT, with 60nm Au nanoparticles drop-cast on top. The molecule length sets the 1.3nm spacing (*18*), giving resonances which are experimentally measured with visible and MIR light (Fig. 1C). Comparing with simulations shows field enhancements E/E_0 >500 (visible) and >200 (MIR) (Fig. S4A) (*19*), providing a more favourable geometry than previously devised for (simulating) molecular upconversion (*17*). A modified microscope focusses visible and MIR lasers onto the same NPoR device (with >40 NPoRs tested here). The 1080cm^{-1} molecular vibration is observed in SERS antiStokes emission, with amplitude that increases linearly when pumped directly with MIR radiation tuned to the same energy.

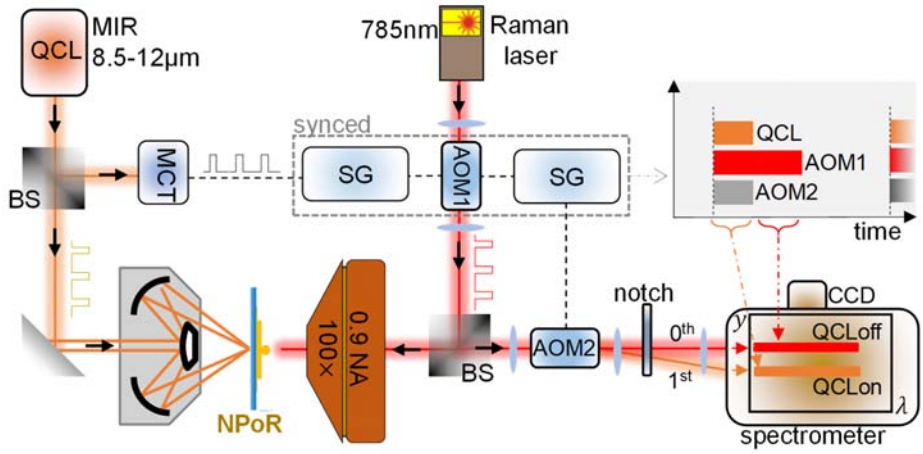

Fig. 2. MIR and visible spectroscopy. Dual microscope combines visible probe and MIR pump for frequency upconversion of molecules in nanogaps: AOM (acousto-optical modulator), MCT (mercury-cadmium-telluride detector), BS (beamsplitter), SG (signal generator). Inset: Timing sequence of each repetition of QCL (pump) to Raman laser modulation (AOM1), where AOM2 deflects SERS spectrum to different vertical position y on spectrometer slit.

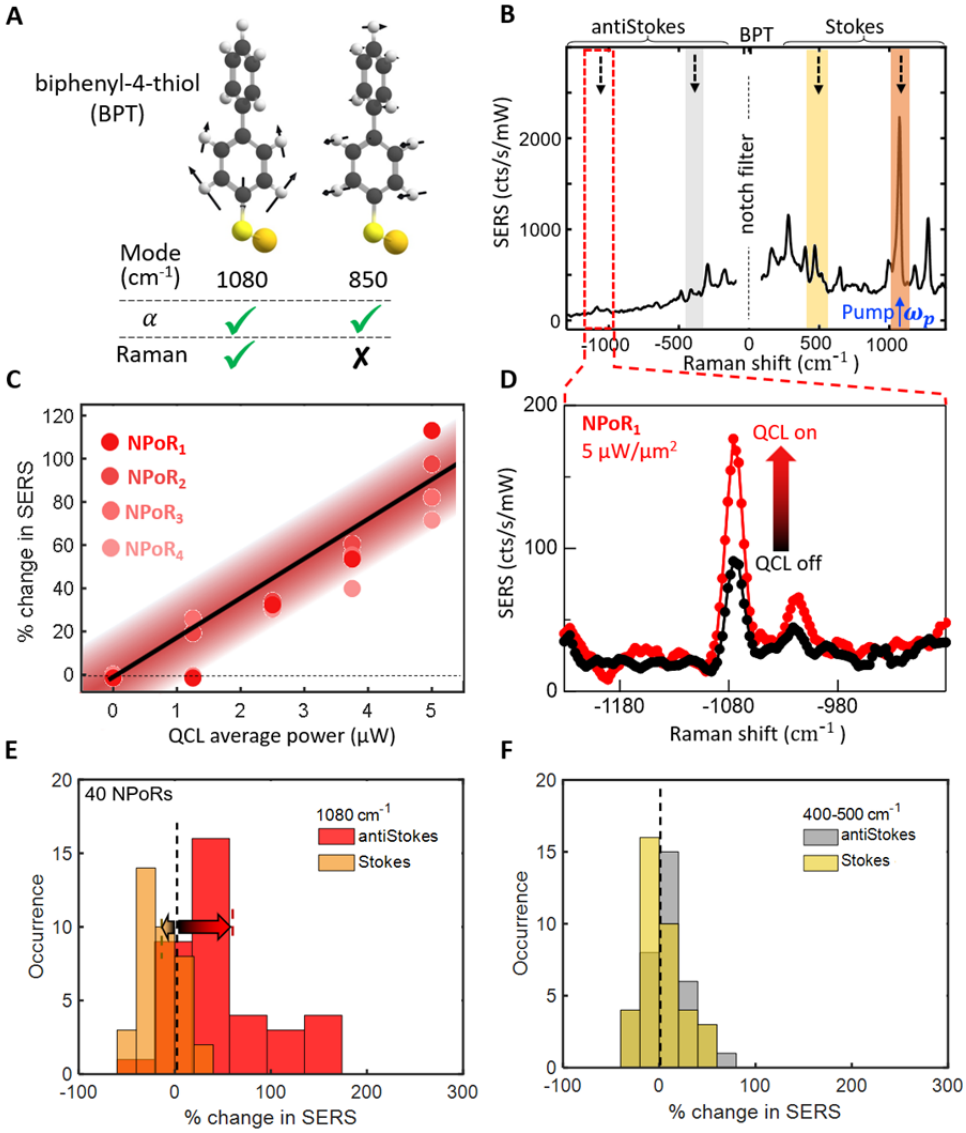

Fig. 3. Upconversion of MIR to visible photons in hybrid plasmonic antennas. (**A**) Vibrations of BPT, showing frequencies with strong infrared absorption (α) or Raman. (**B**) BPT SERS spectrum from 785 nm probe alone. Shaded regions mark pump (orange, 1080cm^{-1}) and monitored frequency bands (arrows). (**C**) Power dependence for 4 NPoRs. (**D**) Raw spectra showing ν=1080cm^{-1} antiStokes increase when MIR pump is on (red). (**E-F**) MIR-induced change in SERS of 40 NPoRs at Stokes and antiStokes peaks at (E) 1080cm^{-1} and (F) 400-500cm^{-1}.

Our experiments use synchronised visible and quantum cascade laser (QCL) rectangular pulses (0.4 μs) to collect SERS spectra with/out the MIR light (Fig. 2). These confirm the prediction of upconversion (*17*), using the ν=1080cm^{-1} BPT mode which is both infrared and Raman active (Fig. 3A, 4A). Measuring SERS from NPoRs shows the expected BPT vibrations on both Stokes and antiStokes sides of the laser (Fig. 3B), which are stable and repeatable over long periods. The QCL is then tuned to the same photon energy $h\nu$ (orange, Fig. 3B) and an infrared pump power dependence recorded (Fig. 3C). We find that the antiStokes SERS is 200% higher when QCL average powers of 5μW/μm^2 are incident (Fig. 3D, using peak area

ratio $\mathrm{AS(QCL_{on})/AS(QCL_{off})}$ with background-subtracted antiStokes peaks, see Methods, S2). The expected linear dependence of frequency upconversion with pump power is similar for different NPoRs (red points, Fig. 3C). The lowest detectable light intensity of these dual-wavelength plasmonic antennas is $\sim 1\mu W/\mu m^2$ (Fig. 3C), while the lock-in detection synchronised technique here shows that the response speed is sub-µs, much faster than the QCL pulse repetition rate (5 µs).

To better quantify the upconversion efficiency, we measure the percentage change of SERS on 40 NPoRs, where each NP is located at different positions on its disk antenna. These show an average 52% increase of antiStokes at ν (red, Fig. 3E) for $5\mu W/\mu m^2$ MIR, while by contrast the Stokes at ν shows a decrease of 13% (red). No systematic correlation with the NP position on the disk is apparent, though likely it controls in-coupling of both visible and MIR light into the nanogap.

To confirm the frequency upconversion mechanism, the % SERS changes are also extracted for the 400-500cm^{-1} spectral region (yellow/grey shaded areas for Stokes/antiStokes, Fig. 3B). These low frequency vibrational modes show no discernible change within the ±10% signal noise (Fig. 3F). This lack of low wavenumber signal shows that the signal is not simply thermal heating (Fig. S5), as also suggested by the sub-µs response, but instead is a non-equilibrium response. If simple heating were involved, a trebling of antiStokes at 1080cm^{-1} would give a 60% increase at 450cm^{-1}, which is not observed.

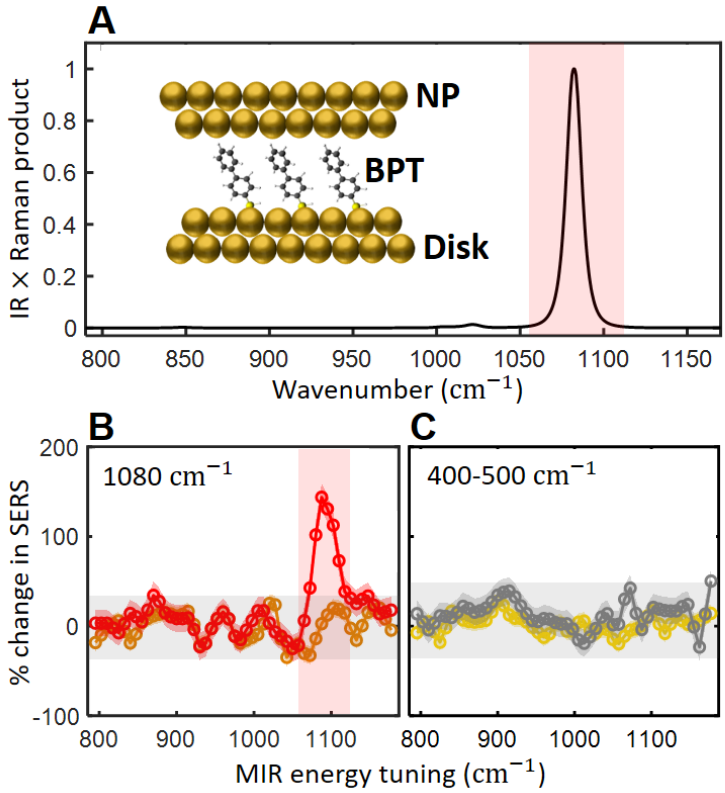

Fig. 4. MIR tuning dependence of upconversion in NPoR plasmonic construct. (**A**) Calculated product of molecular infrared absorption and Raman cross-section for BPT in plasmonic nanogaps (inset). (B-

C) Percentage change in SERS from illuminated NPoR *vs* MIR frequency. Orange (yellow) and red (grey) correspond to SERS change of (**B**) 1080cm^{-1} and (**C**) 400-500cm^{-1} Stokes and antiStokes peaks.

To understand the frequency-selective dependence, we calculate the product of infrared absorption and Raman intensity of BPT, averaged over all orientations for each normal mode (Fig. 4A, SI section S1) (*22*). This clearly shows that the optimum overlap of optical and vibrational modes is at 1080cm^{-1}, and that the dipoles are all well-aligned with the vertical E field in the nanogap at both visible and MIR wavelengths. To confirm this, we tune the QCL from 795-1170cm^{-1} in 15cm^{-1} steps, ensuring a constant 5μW/μm^2 incident on the sample. While the NPoR device shows a resonant antiStokes increase of 140% at 1080cm^{-1} it shows no increase elsewhere across the frequency scan (red, Fig. 4B), and neither does the Stokes signal (orange). No clear change in SERS intensity is also seen for the 400-500cm^{-1} lines across this MIR tuning on the same NPoR (Fig. 4C). This data clearly distinguishes the direct resonant pumping of the optimum 1080cm^{-1} mode.

The quantum efficiency of these devices is estimated by calibrating to the thermal scale of antiStokes emission. At room temperature (T=300K), with MIR powers of P=100μW (intensity I =5μW/μm^2) at 1080cm^{-1} ($h\nu$=0.13eV), and assuming decay times from the first vibrational state of τ=1 ps (*20, 23*), using the measured antiStokes increase of Δζ =100% (see Fig. 3C) gives the fraction of MIR photons arriving that produce an observed vibration excitation as

$$\eta = \Delta\zeta \exp\left\{-\frac{h\nu}{k_B T}\right\}\left[\left(\frac{P}{h\nu}\right)\tau\right]^{-1} \qquad (1)$$

corresponding to photon quantum efficiency η∼2x10^{-6} in this first generation of devices. The induced occupation of the first vibrational level is estimated to be $\Delta\zeta \exp\{-h\nu/k_B T\}$ ∼1%. This should be compared with the theoretical estimate (*17*),

$$\eta = \eta_{\mathrm{IR}} \frac{g^2 \tau}{\kappa_{\mathrm{IR}}} \sim 1 \times 10^{-6} \qquad (2)$$

using the measured MIR linewidth (Fig. 1C) to get the antenna loss rate κ_{IR}∼2.7THz, an antenna efficiency η_{IR}∼0.5 and an optomechanical coupling g∼2GHz for BPT molecules in the nanocavity gap (*20, 21*). This assumes that the optical cross-section of the dual-wavelength antenna matches the incident MIR focus. The main inefficiency is in the fraction of MIR photons giving significant field inside the NPoR gap to vibrationally excite a molecule. Improving the Q factor of the antenna, for example using hybridization with photonic cavities, is needed for further enhancements (*24*).

We also show it is possible to fabricate these integrated NPoR detectors using SiN waveguides on standard 4" Si wafers (*25*), by cheap and scalable combination of top-down and bottom-up lithographies (Fig. S3). Prospects for wideband operation are promising, with lower frequency antiStokes emission already observed at 250cm^{-1} (see Fig. 3B, λ=40μm or 7.5 THz). Utilising alternative molecules embedded in NPoRs, SERS lines observed ∼160cm^{-1} access targets for astronomical detectors (OH line at 4.7THz and lower). Although the lifetime of such devices is not yet fully characterised, it already exceeds 1 week, depending on suitable encapsulation to exclude oxygen. The rapid relaxation of non-resonant molecules in the

virtual Raman process is encouraging for engineering robust performance. We emphasise further increases in sensitivity can come from exploiting single-atom picocavities, which deliver hundred-fold larger SERS signals from the enhanced light localisation around single Au adatoms (*26, 27*), with simple estimates based on eqn (2) using the measured $g \sim 5$THz (*20, 21*) giving near unity upconversion efficiencies. This makes current efforts to stabilise picocavities significant, as well as optimising the overlap of MIR light in the same volume.

REFERENCES AND NOTES

1. M. J. Elrod, Greenhouse warming potentials from the infrared spectroscopy of atmospheric gases. *J. Chem. Educ.* **76**, 1702 (1999).
2. A. Kuze, H. Suto, M. Nakajima, T. Hamazaki, Thermal and near infrared sensor for carbon observation Fourier-transform spectrometer on the Greenhouse Gases Observing Satellite for greenhouse gases monitoring. *Appl. Opt* **48**, 6716-6733 (2009).
3. R. S. Allison, J. M. Johnston, G. Craig, S. Jennings, Airborne optical and thermal remote sensing for wildfire detection and monitoring. *Sensors* **16**, 1310 (2016).
4. W. R. Bandeen, R. Hanel, J. Licht, R. Stampfl, W. Stroud, Infrared and reflected solar radiation measurements from the TIROS II meteorological satellite. *J. Geophys. Res.* **66**, 3169-3185 (1961).
5. R. Hanel *et al.*, The Nimbus 4 infrared spectroscopy experiment: 1. Calibrated thermal emission spectra. *J. Geophys. Res.* **77**, 2629-2641 (1972).
6. A. Rogalski, Infrared detectors: an overview. *Infrared Phys. Technol.* **43**, 187-210 (2002).
7. J. S. Dam, P. Tidemand-Lichtenberg, C. Pedersen, Room-temperature mid-infrared single-photon spectral imaging. *Nat. Photonics* **6**, 788-793 (2012).
8. I. Kviatkovsky, H. M. Chrzanowski, E. G. Avery, H. Bartolomaeus, S. Ramelow, Microscopy with undetected photons in the mid-infrared. *Sci. Adv.* **6**, eabd0264 (2020).
9. S. Junaid *et al.*, Video-rate, mid-infrared hyperspectral upconversion imaging. *Optica* **6**, 702-708 (2019).
10. M. Forsch *et al.*, Microwave-to-optics conversion using a mechanical oscillator in its quantum ground state. *Nat. Physics* **16**, 69-74 (2020).
11. J. Bochmann, A. Vainsencher, D. D. Awschalom, A. N. Cleland, Nanomechanical coupling between microwave and optical photons. *Nat. Physics* **9**, 712-716 (2013).
12. W. Jiang *et al.*, Efficient bidirectional piezo-optomechanical transduction between microwave and optical frequency. *Nat. Communications* **11**, 1-7 (2020).
13. L. Shao *et al.*, Microwave-to-optical conversion using lithium niobate thin-film acoustic resonators. *Optica* **6**, 1498-1505 (2019).
14. F. Yesilkoy *et al.*, Ultrasensitive hyperspectral imaging and biodetection enabled by dielectric metasurfaces. *Nat. Photonics* **13**, 390-396 (2019).
15. A. Tittl *et al.*, Imaging-based molecular barcoding with pixelated dielectric metasurfaces. *Science* **360**, 1105-1109 (2018).
16. B. Schwarz *et al.*, Monolithically integrated mid-infrared lab-on-a-chip using plasmonics and quantum cascade structures. *Nat. Communications* **5**, 1-7 (2014).
17. P. Roelli, D. Martin-Cano, T. J. Kippenberg, C. Galland, Molecular Platform for Frequency Upconversion at the Single-Photon Level. *Phys. Rev. X* **10**, 031057 (2020).
18. J. J. Baumberg, J. Aizpurua, M. H. Mikkelsen, D. R. Smith, Extreme nanophotonics from ultrathin metallic gaps. *Nat. Materials* **18**, 668-678 (2019).
19. A. Xomalis *et al.*, Interfering Plasmons in Coupled Nanoresonators to Boost Light Localization and SERS. *Nano Lett.* **21**, 2512-2518 (2021).

20. A. Lombardi *et al.*, Pulsed Molecular Optomechanics in Plasmonic Nanocavities: From Nonlinear Vibrational Instabilities to Bond-Breaking. *Phys. Rev. X* **8**, 011016 (2018).
21. F. Benz *et al.*, Single-molecule optomechanics in "picocavities". *Science* **354**, 726-729 (2016).
22. Z. Koczor-Benda *et al.*, Molecular Screening for Terahertz Detection with Machine Learning-based Methods. *In Review*, (2021).
23. S. Yampolsky *et al.*, Seeing a single molecule vibrate through time-resolved coherent anti-Stokes Raman scattering. *Nat. Photonics* **8**, 650-656 (2014).
24. A. I. Barreda *et al.*, Hybrid Photonic-Plasmonic Cavities based on the Nanoparticle-on-a-Mirror Configuration. *arXiv preprint: 2106.01931 (2021)*, (2021).
25. J. Losada *et al.*, SERS Detection via Individual Bowtie Nanoantennas Integrated in Si_3N_4 Waveguides. *IEEE J. Sel. Top. Quantum Electron.* **25**, 1-6 (2019).
26. T. Wu, W. Yan, P. Lalanne, Bright plasmons with cubic nanometer mode volumes through mode hybridization. *ACS Photonics* **8**, 307-314 (2021).
27. T. Wu, M. Gurioli, P. Lalanne, Nanoscale Light Confinement: the Q's and V's. *ACS Photonics*, (2021).

ACKNOWLEDGMENTS

Funding: We acknowledge support from European Research Council (ERC) under Horizon 2020 research and innovation programme THOR (829067), POSEIDON (861950) and PICOFORCE (883703). We acknowledge funding from the EPSRC (Cambridge NanoDTC EP/L015978/1, EP/L027151/1, EP/S022953/1, EP/P029426/1, and EP/R020965/1). X.Z. acknowledges support from KU Leuven Internal Funds C14/19/083, IDN/20/014, KA/20/019 and FWO G090017N. R.C. acknowledges support from Trinity College, University of Cambridge. Z.K.B. and E.R. acknowledge funding from EPSRC (EP/R013012/1, EP/L027151/1) and ERC project 757850 BioNet. We are grateful to the UK Materials and Molecular Modelling Hub for computational resources, which is partially funded by EPSRC (EP/P020194/1). **Author contributions:** AX fabricated the devices, performed the experiments and data analysis. ZX obtained analytical electromagnetic calculations. RC and AX did full-wave simulations. SKB performed DFT calculations. EM and AX performed SERS of NPoR on Si chips. ER, AM, JJB designed and supervised the work. All authors discussed the results, provided feedback and contributed to the writing of the manuscript. **Competing interests:** The authors declare no competing financial interest**. Data and materials availability:** All data needed to evaluate the conclusions in the study are present in the main text or the supplementary materials. Source data can be found at:

SUPPLEMENTARY MATERIALS

Publications website at DOI:

Materials and Methods

Supplementary Text

Figs. S1 to S7

Science
AAAS

Supplementary Materials for

Detecting mid-infrared light by molecular frequency upconversion with dual-wavelength hybrid nanoantennas

Angelos Xomalis [1], Xuezhi Zheng [1,2], Rohit Chikkaraddy [1], Zsuzsanna Koczor-Benda [3], Ermanno Miele [1,4,5], Edina Rosta [3], Guy A E Vandenbosch [2], Alejandro Martínez [6], Jeremy J Baumberg [1*]

[1] NanoPhotonics Centre, Cavendish Laboratory, Department of Physics, University of Cambridge, Cambridge, United Kingdom.
[2] Department of Electrical Engineering (ESAT-TELEMIC), KU Leuven, Leuven, Belgium.
[3] Department of Physics and Astronomy, University College London, London, United Kingdom.
[4] Department of Chemistry, University of Cambridge, Cambridge, United Kingdom
[5] The Faraday Institution, Harwell Science and Innovation Campus, Oxford, United Kingdom
[6] Nanophotonics Technology Center, Universitat Politècnica de València, Valencia, Spain.

Correspondence to: jjb12@cam.ac.uk

This PDF file includes:

Materials and methods

Self-assembled nanogaps in dual-wavelength antennas. We fabricate an array of disk resonators using a laserwriter with source at 375nm wavelength (ProtoLaser LDI, LPKF) on a positive photoresist and develop the exposed resist with deionized (DI) water. Next, we deposit 100 nm of Au with an E-beam evaporator (at 0.5 nm/s, Kurt J. Lesker) and then to lift-off the Au-coated resist, we dip the samples in an acetone solution for 2 h. We then immerse the disk resonator arrays in 1 mM biphenyl-4-thiol (BPT, Sigma Aldrich, 97%) solution in anhydrous ethanol (Sigma Aldrich, <0.003% H_2O) for 12 h to create SAMs that are defined by the length of the molecule (1.3 ± 0.1 nm for BPT). Lastly, citrate-capped 60 nm Au NPs (BBI Solutions) are deposited by drop casting on the BPT-coated Au-disks. The excess of NPs is flushed off with DI water.

Computational electromagnetics method (CEM). Our computational method uses a Volume Integral Equation (VIE) formalism of Maxwell's equations (*1*). The VIE is numerically solved by the Volumetric Method of Moments (V-MoM) algorithm to find volumetric currents flowing in the nano-objects. Further near- and far-field can be derived by using Green functions. The V-MoM algorithm uses tetrahedral or hexahedral mesh to find volumetric currents (*2, 3*). V-MoM methods only discretizes the volume of the nano-objects and not the surrounding elements and thus demand 100-fold less computational resources compared to finite-difference time-domain (FDTD) and finite element methods (FEM) for similar accuracy results (*4*).

MIR and visible spectroscopy. We perform dual-wavelength spectroscopy with a modified optical microscope (Olympus BX51) with tuneable MIR radiation (8.5-12.6 μm) simultaneous with a 785 nm Raman laser (Matchbox, Integrated Optics) on single nanostructures. We estimate the focal spot diameter of visible light on the sample to be around 1 μm^2 and the MIR to be 20 μm^2 (depending on the exact MIR wavelength). To enhance the visible and MIR light overlap, we fix the timescales of the two sources by triggering AOM1 from a MCT detector that detects a fraction of the 400 ns pulses of the infrared QCL (Laser Tune, Block Engineering) with a repetition rate of 0.2 MHz. We set the pulses of the visible (probe) to 800 ns long and MIR (pump) to 400 ns (see timing diagram Fig. 2 inset). In the detection arm, we install a second AOM2 that is synchronized to AOM1 and splits the inelastically-scattered light pulse into two equal parts which are gated in time (Fig. 2). The first window overlaps with the MIR laser ($\mathrm{QCL_{on}}$) and second window with the MIR off which is used as a reference ($\mathrm{QCL_{off}}$). AOM2 deflects $\mathrm{QCL_{on}}$ into the 1st diffraction order while $\mathrm{QCL_{off}}$ transmits only in the 0th order. With a pair of lenses, we collimate both 0th and 1st diffracted orders and focus onto the spectrometer (Andor Shamrock i303) and a Newton EMCCD camera. The two spots, are separated at different vertical heights on the spectrometer slits, and thus can be extracted and processed (after calibration) to give separate spectra (see control experiment S7). This detection scheme can be checked to ensure quantitative performance. In this way, we achieve one-shot-measurements that acquire both signal and reference SERS spectra, taken at the same time. This is of vital importance as every signal is now referenced and thus excludes any slow thermal effects or mechanical drift. This nanosecond lock-in detection delivers higher signal-to-noise ratio. Samples are fabricated on 150 μm thick Si substrates

semi-transparent for this MIR wavelength range and placed onto a motorised stage controlled by in-house Python code that allows automated measurements of many individual nanostructures (*5-7*). In all SERS measurements, the 785nm laser intensity is 200 μW/μm^2 with total 10 sec integration time. In Fig. 3D,4B-C) the experimental data interpolated by a factor of 2.

S1 Calculation of infrared absorption and Raman intensity

Calculations for single biphenyl-4-thiol (BPT) molecule were performed at the B3LYP/aug-cc-pVTZ level with D3 dispersion correction using the Gaussian program package. The thiol hydrogen was exchanged to a single gold atom, following the methodology in Ref. (*8*). Infrared (IR) absorption, Raman intensity and their product were calculated as described in Ref.(*8*), with a frequency scaling of 0.98 and broadening of FWHM=15 cm^{-1} (17 cm^{-1}) for Raman (IR) spectra (derived from experimental measurements).

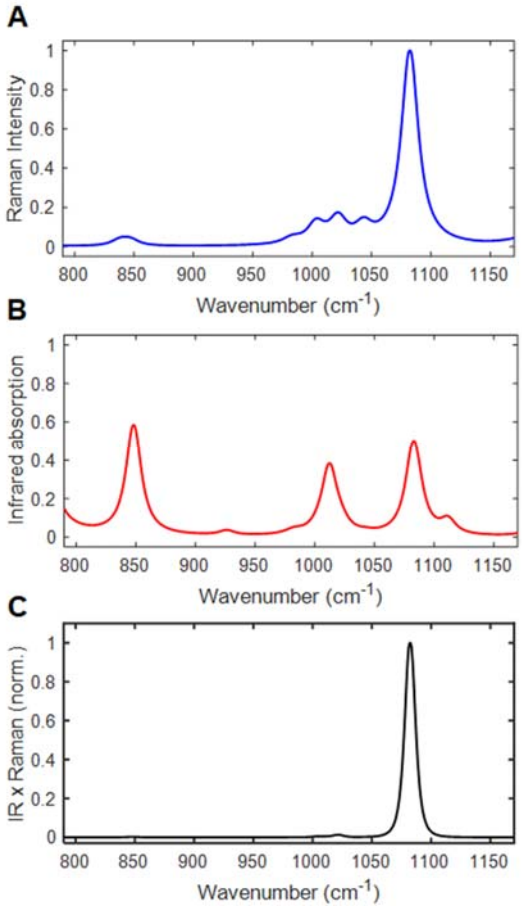

Fig. S1: Calculation of infrared absorption and Raman intensity of BPT. Normalised intensities of (**A**) Raman, (**B**) infrared absorption and (**C**) their product.

S2 Power dependence of Nanoparticle-on-resonator (NPoR).

For clarity, we show the infrared pump power dependence for other frequency bands (Fig. S2). We find that the 1080 cm^{-1} antiStokes SERS (using peak area ratio $AS(QCL_{on})/AS(QCL_{off})$ for background-subtracted antiStokes peaks, see Methods) is 200% higher when QCL average powers of 5 $\mu W/\mu m^2$ are incident (Fig. 3C). By contrast the Stokes for ν=1080 cm^{-1} and Stokes and antiStokes for 400-500 cm^{-1} show no discernible change.

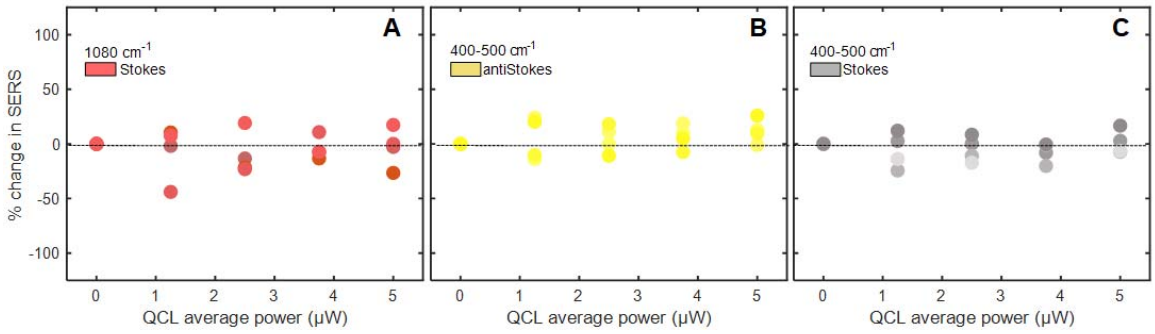

Fig. S2: Power dependence of Nanoparticle-on-resonator (NPoR). Power induced change in SERS for 4 NPoRs at Stokes and antiStokes peaks at (**A**) 1080 cm^{-1} and (**B-C**) 400-500 cm^{-1}.

S3 Waveguide integrated nanostructures on a silicon chip for SERS.

We present preliminary studies on dual-resonant antennas integrated with SiN waveguides on Si chips. Waveguides assist laser illumination and collection of inelastically-scattered light (Fig. S3A). Au nanoparticles can be successfully drop-cast on top of the disks, forming nanogaps (Fig. S3B). Light coupled into the waveguide excites the NPoR antenna at its end and BPT SERS is collected back (Fig. S3C-D). Currently further studies are on-going to investigate the full behaviour of the SERS light, and integration with the MIR sources.

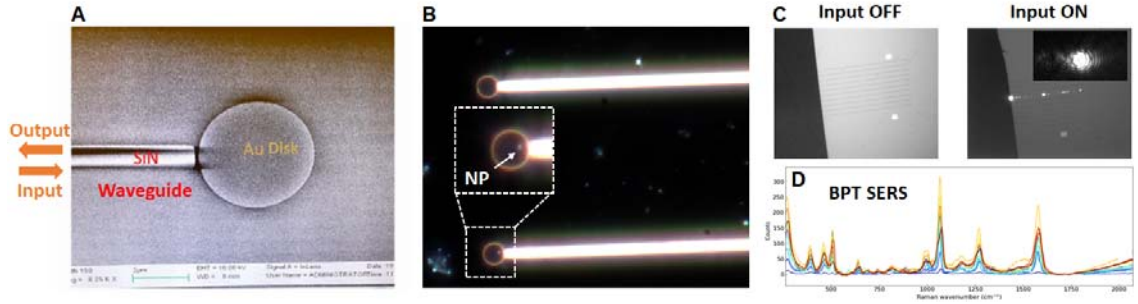

Fig. S3 Chip-integrated plasmonic antennas for SERS spectroscopy. (**A**) A SiN waveguide (0.65 μm width) is fabricated abutting a 6 μm Au disk resonator. The waveguide assists laser illumination and collection of SERS light from the disk. (**B**) Self-assembled monolayer of biphenyl-4-thiol (BPT) creates 1.3 nm cavity between 60 nm Au nanoparticle and disk. (**C**) Laser light couples into the waveguide and excites the NPoR at the end. Inset shows the disk upon illumination. (**D**) BPT SERS Stokes spectrum from 785 nm probe. Colors correspond to different waveguides.

S4 Scattering and near-field of NPoR at mid-infrared (MIR) frequencies.

As discussed in Methods here we use V-MoM to calculate the total scattering and near-field *vs* incident angle of incoming light (Fig S4). We consider 6 µm Au disk resonator and a nanoparticle placed at a radial position of 2.7 µm on the disk. "0 degree" corresponds to normal incidence.

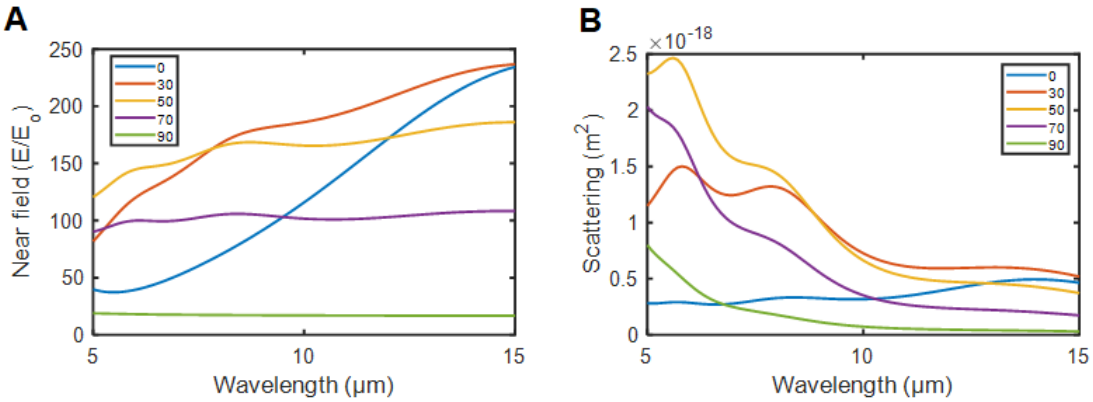

Fig. S4 Scattering and near-field of NPoR at the MIR range. (**A**) Total scattering intensity and (**B**) near-field in the nanogap of a nanoparticle placed at a radial position of 2.7µm on a 6 µm Au disk resonator *vs* incident angle of incoming light. Colors correspond to different angles.

S5 Optical photothermal simulations:

Here we calculate the optical heating to investigate that the signals are not simply thermal heating but instead arise from a non-equilibrium response. First we calculate with a full-wave solver (FDTD) the MIR optical absorption of the NPoR and import this into a thermal solver (Lumerical) using methods and material thermal conductivities extracted previously (*7, 9*). The NPoR retains more heat when illuminated with the probe beam (785 nm) from top, rather than from the pump (10 µm) from the bottom due to the lower coupling to the nanogap as well as its power (Fig. S5). For our simulations, we use ambient temperature (300 K) irradiation at 785 nm and 10 µm and optical intensities 0.2 and 0.1 mW/µm^2 respectively. Our findings are in a good agreement with previous published results and show that such nanogap plasmonic constructs neither show a thermal gradient in the metal as this dissipates, nor activate atomic migration at that power levels (*7*). This ensures stable nanoparticle facets and upconversion measurements. Thus these results also confirm that the average antiStokes increase (52%) is not originating from photothermal effects from the MIR pump (Fig. 3E).

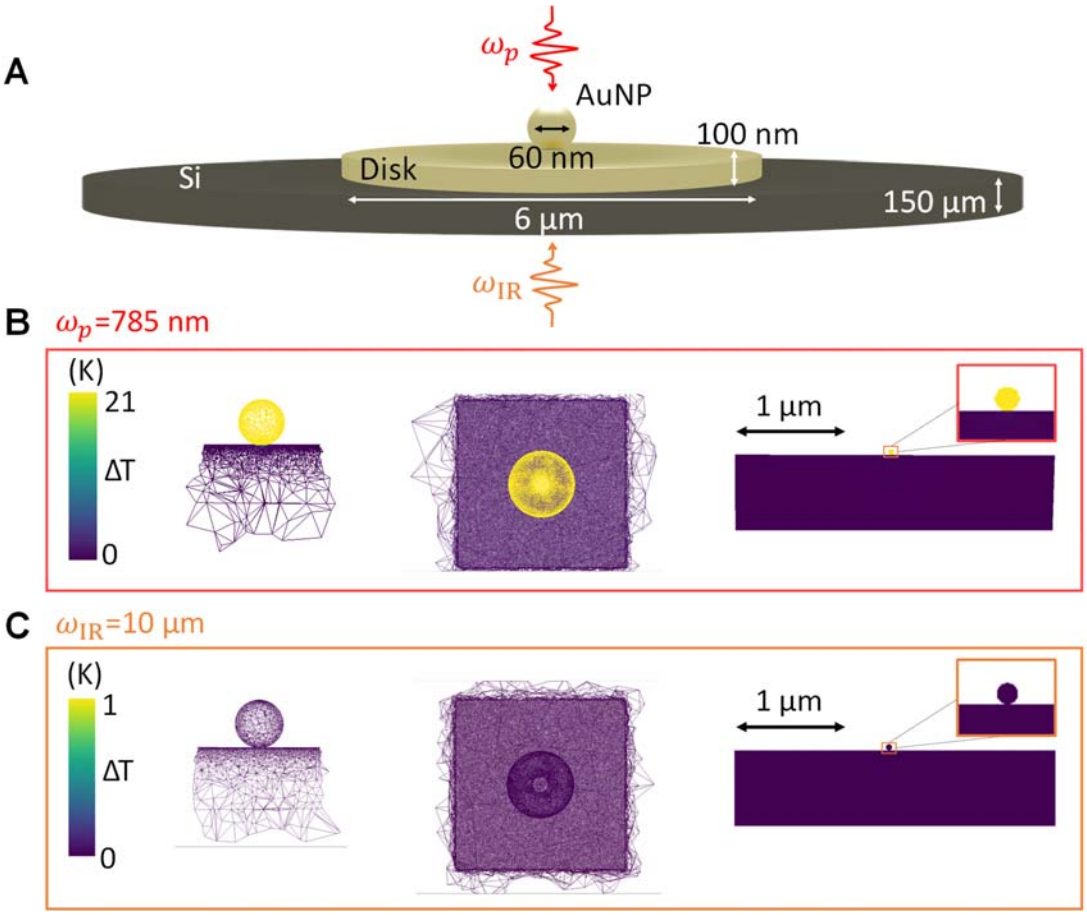

Fig. S5 Local photothermal heating calculations on NPoR. (**A**) NPoR schematic with dual illumination. (**B-C**) Optically induced heating for (B) probe beam of 785 nm and (C) pump beam of 10 µm. (left) Cross-section, (middle) top surface and (right) large area cross-section. Ambient temperature irradiation is at 785 nm and 10 µm and optical intensity is at 0.2 and 0.1 mW/µm^2 respectively.

S6 Frequency upconversion control experiment:

As we discussed in Methods (MIR and visible spectroscopy section) inelastic scattered light is directed to the AOM2 which deflects $\mathrm{QCL_{on}}$ into the 1st diffraction order while $\mathrm{QCL_{off}}$ transmits only in the 0th order. With a pair of lenses, we collimate both 0th and 1st diffracted orders and focus onto the spectrometer and EMCCD camera. Here for clarity, we show spectra recorded with the same methodology but now QCL is been blocked (Fig. S6). The two spots give separate spectra (blue and green). In contrast to Fig. 3D) there is no change in the 1080 cm^{-1} antiStokes. This validates that the antiStokes increases only when MIR pump is on. Further SERS shows no change for the 400-500 cm^{-1} spectral region.

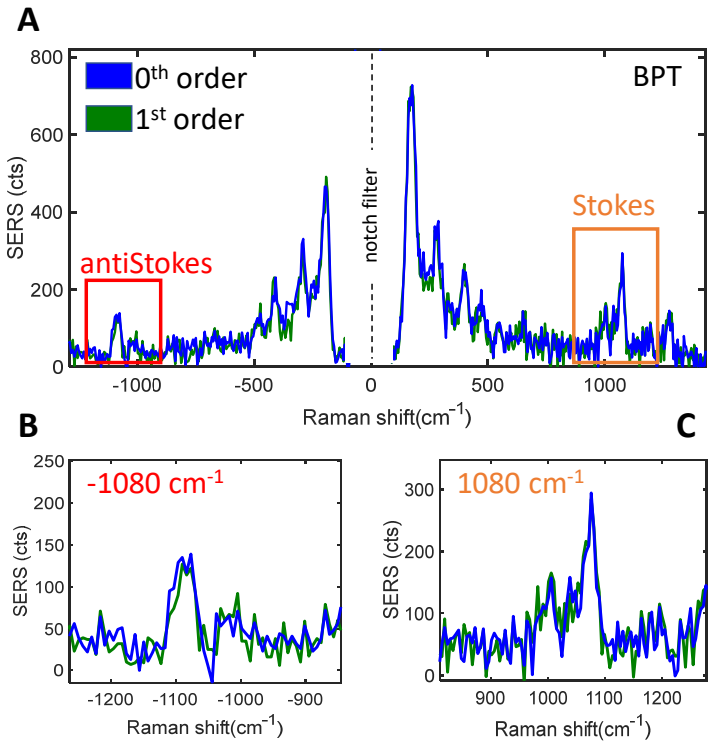

Fig. S6 Upconversion control experiment. (**A**) SERS spectra of BPT of 0th (blue) and 1st (green) diffracted orders. (**B-C**) Raw spectra showing ν=1080 cm^{-1} (B) antiStokes and (C) Stokes change when MIR pump is off.

S7 SEM characterisation of the NPoRs:

We characterise the NPoR device with scanning electron microscopy (SEM). Here 6 µm diameter Au disks are fabricated on a thin Si substrate (Fig. S6A). Then a monolayer of biphenyl-4-thiol is self-assembled on top, which creates 1.3 nm thick cavities between the 60 nm Au nanoparticles and the Au disk (Fig. S6B).

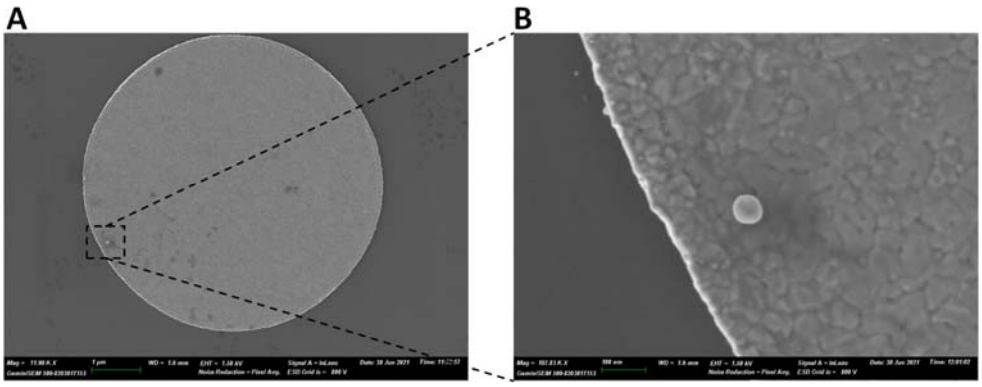

Fig. S7 SEM characterisation of NPoRs. (**A**) 6 µm diameter Au disks on a thin Si substrate. (**B**) 60 nm Au nanoparticle drop cast on the disk.

References

1. X. Zheng, M. Kupresak, N. Verellen, V. V. Moshchalkov, G. A. Vandenbosch, A Review on the Application of Integral Equation-Based Computational Methods to Scattering Problems in Plasmonics. *Adv. Theory Simul.* **2**, 1900087 (2019).
2. D. Schaubert, D. Wilton, A. Glisson, A tetrahedral modeling method for electromagnetic scattering by arbitrarily shaped inhomogeneous dielectric bodies. *IEEE Trans. Antennas Propag.* **32**, 77-85 (1984).
3. X. Zheng *et al.*, Volumetric method of moments and conceptual multilevel building blocks for nanotopologies. *IEEE Photonics J.* **4**, 267-282 (2012).
4. V. K. Valev *et al.*, Nanostripe length dependence of plasmon-induced material deformations. *Opt. Lett.* **38**, 2256-2258 (2013).
5. F. Benz *et al.*, SERS of individual nanoparticles on a mirror: size does matter, but so does shape. *J. Phys. Chem. Lett* **7**, 2264-2269 (2016).
6. M.-E. Kleemann *et al.*, Revealing nanostructures through plasmon polarimetry. *ACS Nano* **11**, 850-855 (2017).
7. A. Xomalis *et al.*, Controlling Optically Driven Atomic Migration Using Crystal-Facet Control in Plasmonic Nanocavities. *ACS Nano* **14**, 10562-10568 (2020).
8. Z. Koczor-Benda *et al.*, Molecular Screening for Terahertz Detection with Machine Learning-based Methods. *In Review*, (2021).
9. Z. J. Coppens, W. Li, D. G. Walker, J. G. Valentine, Probing and controlling photothermal heat generation in plasmonic nanostructures. *Nano Lett.* **13**, 1023-1028 (2013).